Faraday Discussions

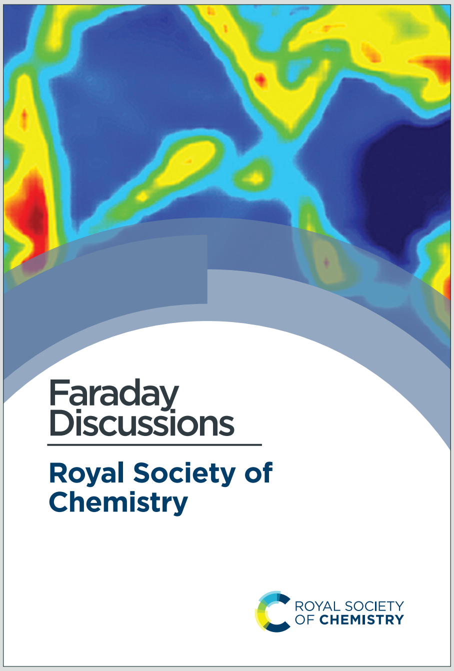

This article can be cited before page numbers have been issued, to do this please use: M. Jaimini Jessica, S. Kundu, L. Yang, L. Wang, M. P. Stockham, B. Spencer and D. Spencer-Jolly, *Faraday Discuss.*, 2026, DOI: 10.1039/D6FD00058D.

ROYAL SOCIETY OF CHEMISTRY

www.rsc.org/faraday_d

Faraday Discussions

View Article Online
DOI: 10.1039/D6FD00058D

PAPER

Solid-liquid electrolyte interphases in quasi-solid-state lithium-sulfur batteries with argyrodite-type solid electrolyte separators

Jaimini Jessica Mistry, [a,b] Sramana Kundu, [d] Lechen Yang, [b,c] Longlong Wang, [e] Mark P. Stockham, [a,b] Ben F. Spencer [d] and Dominic Spencer-Jolly [a,b,*]

a. School of Metallurgy and Materials, University of Birmingham, Pritchatts Road, Birmingham, UK
b. The Faraday Institution, Harwell Science and Innovation Campus, Didcot, UK
c. Department of Materials, University of Oxford, Parks Road, Oxford, UK
d. Henry Royce Institute, Photon Science Institute, Department of Materials, School of Natural Sciences, The University of Manchester, Manchester, UK
e. School of Materials Science and Engineering, Harbin Institute of Technology, Shenzhen 518055, P. R. China

*Corresponding author: d.h.spencer-jolly@bham.ac.uk

Received 00th January 20xx, Accepted 00th January 20xx
DOI: 10.1039/x0xx00000x

Quasi-solid-state lithium-sulfur batteries offer a promising route to combine the high energy density of lithium-sulfur chemistry with improved interfacial stability. However, their performance is limited by the formation of resistive solid-liquid electrolyte interphases at the interface between the solid electrolyte separator and the liquid catholyte. In this work, we investigate solid-liquid electrolyte interphase formation at the interface between an argyrodite-type sulfide solid electrolyte $Li_{5.5}PS_{4.5}Cl_{1.5}$ and two representative liquid electrolytes: a conventional ether-based electrolyte (LiTFSI in DOL:DME) and an ionic liquid (LiTFSI in EMIMTFSI). Using a combination of time-resolved electrochemical impedance spectroscopy, X-ray photoelectron spectroscopy, and focussed ion beam scanning electron microscopy, we reveal substantial differences in interphase chemistry, morphology, and transport properties. The ether-based electrolyte undergoes continuous chemical reaction with the sulfide solid electrolyte, forming a thick, inhomogeneous, and highly resistive interphase (~2,000 $\Omega \cdot cm^2$ after 250 h), driven in part by dissolution of polysulfide species. In contrast, the ionic liquid electrolyte forms a significantly thinner, layered interphase with a comparatively low area-specific resistance (~150–220 $\Omega \cdot cm^2$), which remains constant over extended time and during electrochemical cycling. These findings demonstrate that choice of catholyte plays an important role in governing solid-liquid electrolyte interphase formation, and highlights ionic liquids as viable catholytes for stable, low-resistance interfaces in quasi-solid-state lithium-sulfur batteries with argyrodite-type solid electrolyte separators.

Introduction

Lithium-sulfur (Li-S) batteries are widely regarded as a promising next-generation energy storage technology due to their high theoretical energy density and the natural abundance of sulfur.[1] However, their practical implementation remains constrained by several well-known challenges, including the polysulfide shuttle effect, lithium dendrite growth, and the reliance on sacrificial additives such as $LiNO_3$ to stabilise the lithium metal anode.[2] These issues collectively lead to rapid capacity fade, low Coulombic efficiency, and safety concerns.[3] All-solid-state Li-S batteries offer a potential route to mitigate these challenges by eliminating the liquid electrolyte, thereby suppressing polysulfide dissolution and improving interfacial stability at the lithium metal anode.[4] However, these systems suffer from severe chemomechanical degradation, primarily due to the ~80% volume expansion of the sulfur cathode during lithiation. This induces mechanical stress, interfacial contact loss, and cracking within the all-solid-state cell, ultimately limiting electrochemical performance.[5]

Quasi-solid-state Li-S batteries have emerged as a promising compromise, combining a solid electrolyte separator with a small amount of liquid catholyte.[6,7] In this architecture, the solid electrolyte can inhibit polysulfide shuttling and dendrite propagation,

View Article Online
DOI: 10.1039/D6FD00058D

while the liquid catholyte improves interfacial contact and ionic transport within the cathode. However, this hybrid solid/liquid electrolyte design introduces a new and critical interface between the solid electrolyte and liquid catholyte. Previous studies have found that chemical reactions at this interface are almost unavoidable, leading to the formation of a solid-liquid electrolyte interphase (SLEI).[8] The properties of the SLEI are crucial to device performance: it must exhibit low area-specific resistance and maintain functional stability over extended cycling. Previous studies employing techniques such as X-ray photoelectron spectroscopy (XPS), time-of-flight secondary ion mass spectrometry (ToF-SIMS), Raman spectroscopy, and time-resolved electrochemical impedance spectroscopy (EIS) have demonstrated that SLEIs often consist of poorly conductive decomposition products, significantly contributing to interfacial resistance and overall cell overpotential.[9–16]

To date, most investigations have focused on investigating oxide-based solid electrolytes with various liquid electrolytes.[9,10,13,14,16–29] However, sulfide-based solid electrolytes are attracting increased attention due to their high ionic conductivity, improved dendrite resistance, and lower density - which is particularly advantageous for mass-sensitive applications such as aerospace.[30–32] Early studies have shown that pairing sulfide electrolytes with conventional ether-based liquid electrolytes typically results in the formation of thick, resistive SLEIs due to interfacial instability.[33–35] In contrast, recent work by Vargas-Barbosa and co-workers has demonstrated that ionic liquid electrolytes can enhance interfacial compatibility and reduce SLEI resistance.[31]

In this work, we investigate the interfacial behaviour of the sulfide solid electrolyte $Li_{5.5}PS_{4.5}Cl_{1.5}$ when paired with two different liquid electrolytes: a conventional ether-based electrolyte commonly used in Li-S batteries (LiTFSI in DOL:DME) and an ionic liquid electrolyte (LiTFSI in EMIM-TFSI). Through a combination of microstructural, chemical, and electrochemical characterisation techniques, we demonstrate that the ionic liquid system forms a thinner, more stable SLEI with significantly lower area-specific resistance. These findings highlight the critical role of catholyte selection in engineering stable solid–liquid interfaces and advancing the performance of quasi-solid-state Li-S batteries.

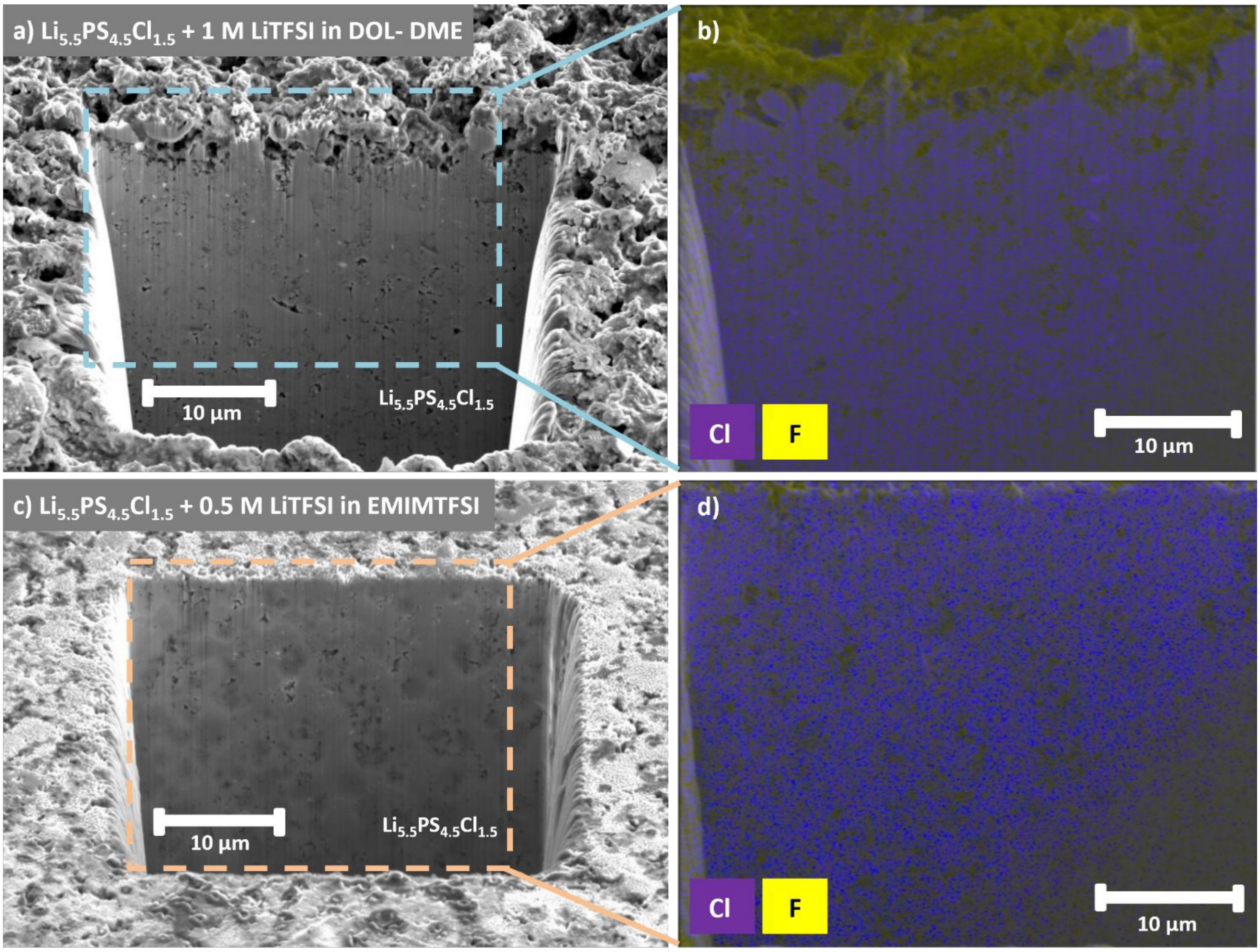

Figure 1: FIB-SEM cross-sectional imaging (a, c) and EDX elemental mapping (b, d) of the $Li_{5.5}PS_{4.5}Cl_{1.5}$ surface after immersion for 250 hours in 1 M LiTFSI in DOL-DME (1:1) (a, b) and in 0.5 M LiTFSI in EMIMTFSI (c, d). b and d show superimposed maps of chlorine (purple) and fluorine (yellow), with additional elemental maps shown in Supplementary Figure 1.

Results and Discussion

Disks of $Li_{5.5}PS_{4.5}Cl_{1.5}$ were prepared as described in the Experimental section, and brought into contact with the two liquid electrolytes; LiTFSI-DOL:DME and LiTFSI-EMIMTFSI. The thickness, chemical composition, and resistance of the SLEIs where characterised by focussed ion beam scanning electron microscopy (FIB-SEM) coupled with energy dispersive X-ray spectroscopy (EDX), time-resolved EIS, and X-ray photoelectron spectroscopy methods (XPS and HAXPES).

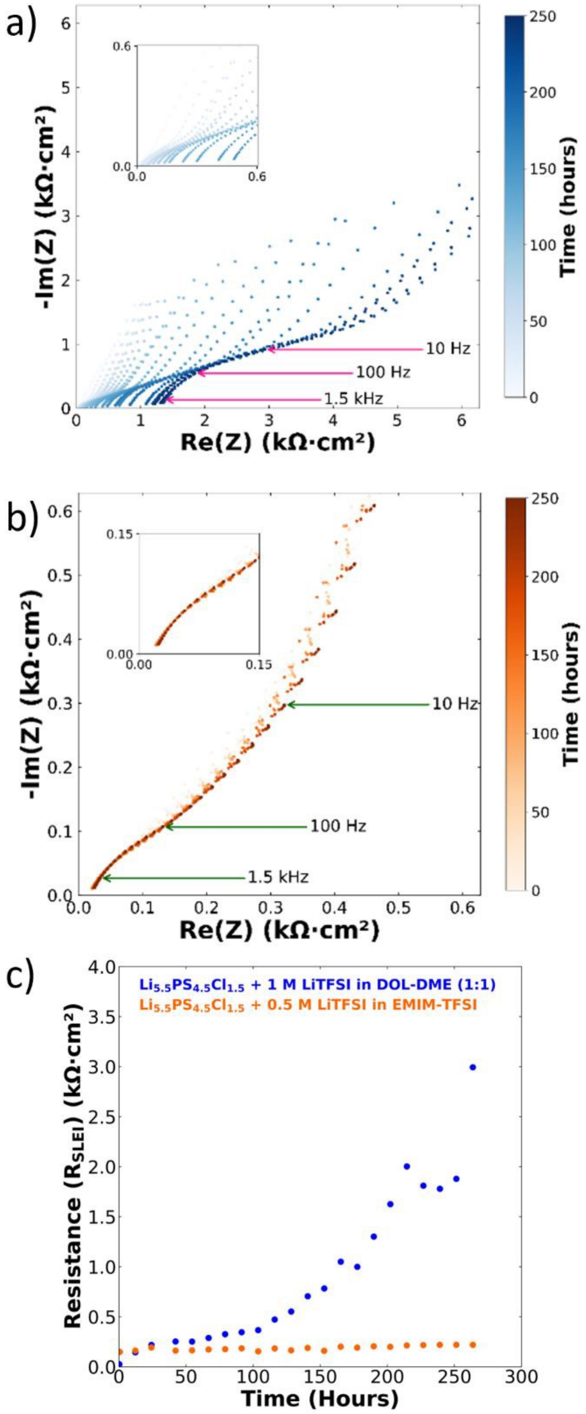

Figure 2: (a, b) Nyquist plots showing time-resolved electrochemical impedance spectroscopy (EIS) of cells with the architecture Blocking Electrode/Liquid Electrolyte/$Li_{5.5}PS_{4.5}Cl_{1.5}$/Liquid Electrolyte/Blocking Electrode over a period of 250 h. a) 1 M LiTFSI in DOL-DME (1:1) (blue). b) 0.5 M LiTFSI in EMIM-TFSI (orange). c) Plot showing evolution of the area-specific resistance of the solid-liquid electrolyte interphase (RSLEI) based on equivalent circuit modelling (Supplementary Figure 2).

$Li_{5.5}PS_{4.5}Cl_{1.5}$/LiTFSI-DOL:DME interphase

Cross-sectional FIB-SEM of the $Li_{5.5}PS_{4.5}Cl_{1.5}$/LiTFSI-DOL:DME interface (Figure 1a) indicates severe chemical degradation and the presence of a heterogeneous interphase. The solid electrolyte surface appears rough and pitted, suggesting that a chemical reaction occurs between the $Li_{5.5}PS_{4.5}Cl_{1.5}$ solid electrolyte and the LiTFSI-DOL:DME liquid electrolyte. Further evidence is apparent in the EDX mapping (Figure 1b), which shows the presence of a chemically-distinct interphase layer which is several microns in thickness. This interphase appears to be fluorine-rich (yellow), but also contains carbon (orange), nitrogen (blue), and oxygen (red), as well as some localised regions of sulfur (green), phosphorous (pink), and chlorine (purple), Supplementary Figure 1. This is distinct from the $Li_{5.5}PS_{4.5}Cl_{1.5}$ bulk material, which shows strong EDX signals for sulfur, phosphorous, and chlorine.

Electrochemical characterisation by time-resolved EIS provides further evidence that a chemical reaction happens between $Li_{5.5}PS_{4.5}Cl_{1.5}$ and the LiTFSI-DOL:DME, forming a resistive interphase. As described in the Experimental section, a two-point probe cell is used to investigate Li-ion transport changes over the solid/liquid electrolyte interface, with the architecture: Blocking Electrode/LiTFSI-DOL:DME/$Li_{5.5}PS_{4.5}Cl_{1.5}$/LiTFSI-DOL:DME/Blocking Electrode. Figure 2a shows the evolution of cell impedance over 250 h without any cell cycling. As time increases (light blue → dark blue), the impedance increases continuously. Each impedance spectrum is fitted to an equivalent circuit model (Supplementary Figure 2), with contributions attributed to: (1) bulk and grain boundary transport processes (modelled together due to overlapping time constants); (2) transport across the solid liquid electrolyte interphase; and (3) the capacitive behaviour of the Blocking Electrode/LiTFSI-DOL:DME interface. This attribution is carried out based on the characteristic capacitances of each transport phenomenon (Supplementary Figure 3), in accordance with the work of Irvine, Sinclair, and West.[36] Fitting to the equivalent circuit model reveals that the increase in the cell resistance with time is due to a substantial increase in the area-specific resistance of the SLEI; increasing from ~25 Ω·cm² to ~2,000 Ω·cm² (Figure 2c).

Finally, XPS used to characterise the chemical species in the solid liquid electrolyte interphase. A $Li_{5.5}PS_{4.5}Cl_{1.5}$ disk, immersed in LiTFSI-DOL:DME liquid electrolyte for 250 hours, is compared against a pristine $Li_{5.5}PS_{4.5}Cl_{1.5}$ sample (Figure 3). Peak assignments are summarised in Table 1. The most substantial changes in the XPS spectra are observed in the S 2p region. The pristine $Li_{5.5}PS_{4.5}Cl_{1.5}$ shows an intense doublet corresponding to the PS_4^{3-} tetrahedron of $Li_{5.5}PS_{4.5}Cl_{1.5}$ (pink). Minor impurities are also observed in the form of Li_2S (purple) and sulfite species (orange). After contact with the liquid electrolyte, there is a significant increase in the relative concentration of sulfite (orange) and sulfate (red) species - indicative of a chemical reaction between the sulfide-type solid electrolyte, and the oxygen-containing

View Article Online
DOI: 10.1039/D6FD00058D

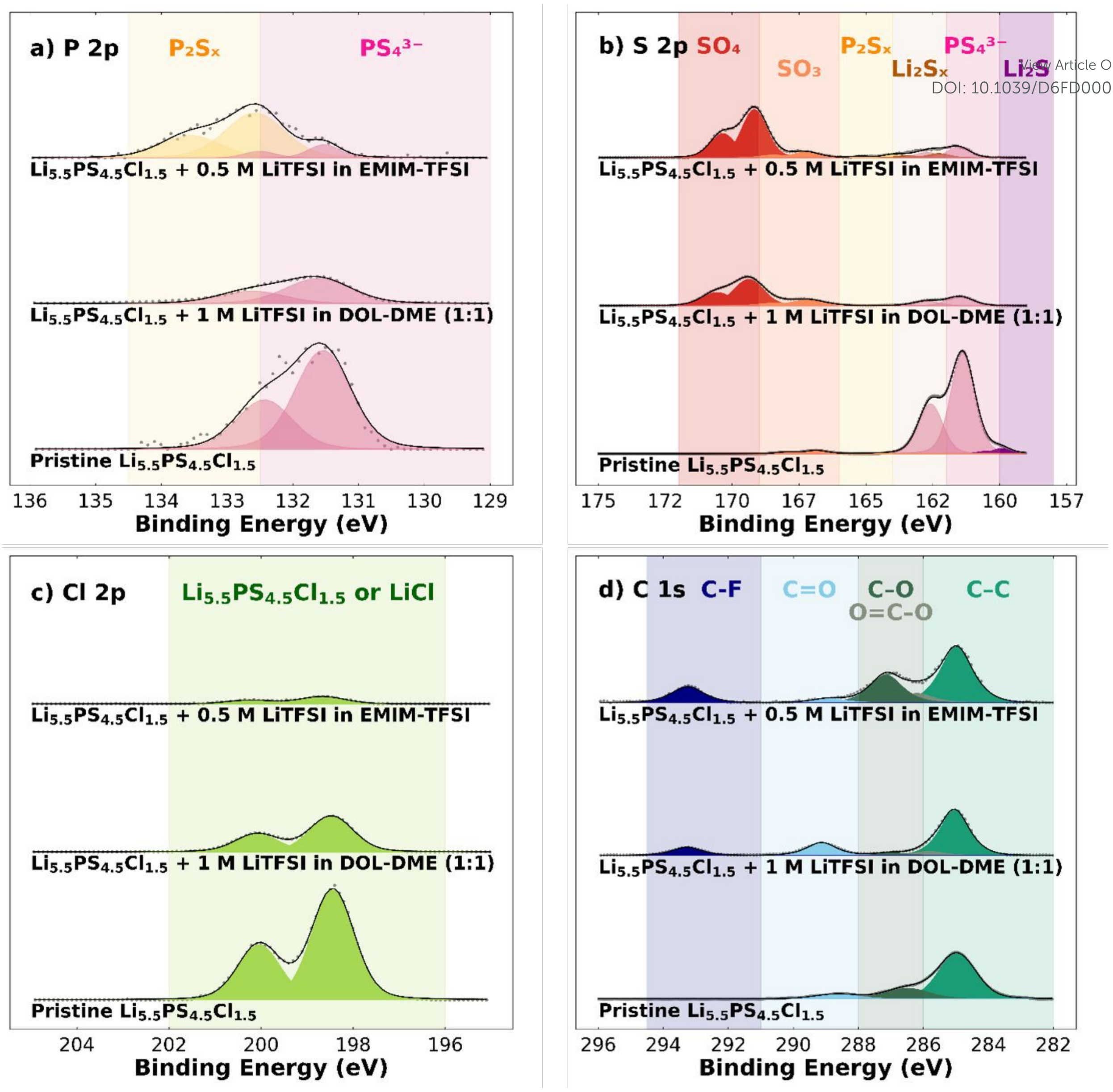

Figure 3: XPS core level spectra of: Pristine $Li_{5.5}PS_{4.5}Cl_{1.5}$ (bottom of each panel), $Li_{5.5}PS_{4.5}Cl_{1.5}$ immersed in 1 M LiTFSI in DOL-DME (1:1) for 250 h (middle), and $Li_{5.5}PS_{4.5}Cl_{1.5}$ immersed in 0.5 M LiTFSI in EMIMTFSI for 250 h (top). a) P 2p region showing P_2S_x (yellow) and PS_4^{3-} (pink). b) S 2p region showing SO_4^{2-} (red), SO_3^{2-} (orange), P_2S_x (yellow), Li_2S_x (brown), PS_4^{3-} (pink), and Li_2S (purple). c) Cl 2p region showing $Li_{5.5}PS_{4.5}Cl_{1.5}$ /LiCl (light green). d) C 1s region showing C-F ($-CF_3$) (dark blue), C=O (light blue), C-O (dark green), O=C-O (grey), and C-C/C-H (teal green). All binding energies are corrected to the C 1s peak at 284.8 eV.

LiTFSI-DOL:DME electrolyte. Other changes were observed in the C 1s region of the spectra, with an increase in C-F containing species (dark blue) after contact with the liquid electrolyte. This is thought to be indicative of precipitation or decomposition of the LiTFSI salt on the surface of the solid electrolyte. No substantial changes are observed in the P 2p or Cl 2p regions of the spectrum. In P 2p, the PS_4^{3-} doublet (pink), is observed in both the pristine and reacted samples, with no other peaks present. In the Cl 2p region of the spectrum, a single doublet (green) is observed in both the pristine and reacted samples. However, it is known that Cl species have very similar binding energies in $Li_{5.5}PS_{4.5}Cl_{1.5}$ and LiCl, and contextually it is thought that LiCl is likely to be formed as a decomposition product, as this is observed in similar systems.[37]

Interestingly, there is no evidence of P_2S_x of Li_2S_x polysulfide species, despite these being expected decomposition products of the reaction between $Li_{5.5}PS_{4.5}Cl_{1.5}$ and LiTFSI-DOL:DME.[33] This is thought to be due to the solubility of these reaction products in the liquid electrolyte, as is known from previous literature. It is possible that the solubility of these polysulfides is responsible for the thick, inhomogeneous, and pitted interphase morphology observed in Figure 1. A plausible mechanism is that as the solid and liquid electrolytes react, the soluble polysulfide products dissolve out of the interphase and into the liquid electrolyte. This creates pathways for liquid electrolyte to react with fresh, unreacted $Li_{5.5}PS_{4.5}Cl_{1.5}$, and this cycle continues until a very thick and resistive solid liquid electrolyte interphase has been formed.

Table 1: Summary of binding energies and assigned chemical species used for the fitting of P 2p, S 2p, Cl 2p and C 1s spectral regions. All binding energies are corrected to the C 1s peak at 284.8 eV.

View Article Online
DOI: 10.1039/D6FD00058D

Spectral Region	Binding Energy (eV)	Species	Colour	Ref
P 2p	132.6	P_2S_X	Yellow	48
	131.6	PS_4^{3-}	Pink	
S 2p	169.0	SO_4	Red	45,[49]
	167.0	SO_3	Orange	
	164.0	P_2S_X	Yellow	
	162.0	Li_2S_X	Brown	
	161.0	PS_4^{3-}	Pink	
	159.0	Li_2S	Purple	
Cl 2p	198.4	$Li_{5.5}PS_{4.5}Cl_{1.5}$/LiCl	Light green	50
C 1s	293.1	C-F	Dark blue	50,51
	288.7	C=O	Light blue	
	286.3	C-O	Dark green	
	286.0	O=C-O	Grey	
	284.8	C-C	Teal green	

We can conclude from chemical, electrochemical, and morphological characterisation of the interphase that the liquid electrolyte, LiTFSI-DOL:DME, is a poor choice to pair with a sulfide-type solid electrolyte such as $Li_{5.5}PS_{4.5}Cl_{1.5}$ in a quasi-solid-state lithium-sulfur battery. Reactivity at the interface appears to be continuous over a period of at least 250 h, as demonstrated by the impedance spectroscopy. What is more, the solid liquid electrolyte interphase is not only very thick (Figure 1 a,b), but composed of highly resistive species including sulfates, sulfites, and various organic decomposition products.

$Li_{5.5}PS_{4.5}Cl_{1.5}$/LiTFSI-EMIMTFSI interphase

In comparison to LiTFSI-DOL:DME, the ionic liquid electrolyte LiTFSI-EMIMTFSI appears considerably less reactive with $Li_{5.5}PS_{4.5}Cl_{1.5}$. Secondary electron imaging (Figure 1c) reveals a surface which is relatively smooth, and the corresponding EDX mapping (Figure 1d) shows a layer which is rich in fluorine (yellow), and carbon (Supplementary Figure 1, orange). This layer is considerably thinner

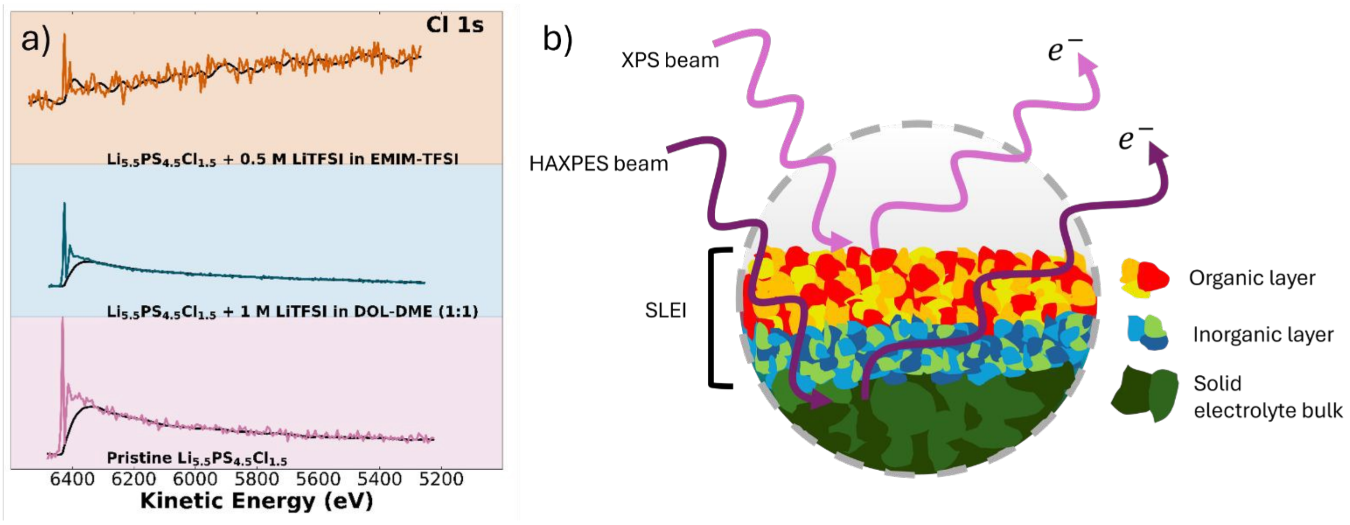

Figure 4: Estimation of Cl-free organic overlayer thickness using HAXPES. a) Core-level HAXPES of the Cl 1s region for: Pristine $Li_{5.5}PS_{4.5}Cl_{1.5}$ (bottom, purple), $Li_{5.5}PS_{4.5}Cl_{1.5}$ immersed in 1 M LiTFSI in DOL-DME (1:1) for 250 h (middle, blue), and $Li_{5.5}PS_{4.5}Cl_{1.5}$ in 0.5 M LiTFSI in EMIMTFSI for 250 h (top, orange). Visual analysis of the background intensity relative to the Cl 1s peak intensity, and fitting of the background, enables estimation of the Cl-free overlayer thickness (see Experimental). b) Schematic showing how HAXPES can be used to estimate the Cl-free organic overlayer thickness. Unlike XPS, HAXPES penetrates 10s of microns into the SLEI, enabling the Cl-free overlayer (yellow/orange/red), to be differentiated from the buried Cl-containing inorganic decomposition layer (blue/green) and the bulk solid electrolyte (green). Fitted HAXPES Cl 1s and S1s spectra are shown in Supplementary Figure 4.

View Article Online
DOI: 10.1039/D6FD00058D

than the interphase observed at the $Li_{5.5}PS_{4.5}Cl_{1.5}$/LiTFSI-DOL:DME interface (Figure 1 a,b) and is thin enough that its thickness cannot be clearly resolved by SEM.

The comparative stability of the interface between $Li_{5.5}PS_{4.5}Cl_{1.5}$ and LiTFSI-EMIMTFSI is also evident from the time-resolved EIS data (Figure 2b). As time increases (light orange → dark red), the impedance of the cell remains relatively unchanged. Equivalent circuit modelling (Supplementary Figure 2) suggests that the area-specific resistance of the SLEI remains low (between 150 $\Omega\cdot cm^2$ and 220 $\Omega\cdot cm^2$) over the 250 h of the measurement (Figure 2c). This SLEI resistance is not only lower than that of the $Li_{5.5}PS_{4.5}Cl_{1.5}$/LiTFSI-DOL:DME interface, but is also lower than other commonly-studied combinations of solid/liquid electrolyte such as between garnet-type oxide ceramics and conventional liquid electrolytes. What is more, it is equivalent in magnitude to other best-in-class combinations, such as the interface between lithium-ion conducting glass ceramic (LiCGC) and LiTFSI-DOL:DME (~70 $\Omega\cdot cm^2$ after 170 h).[16]

While there is little evidence of considerable chemical reactivity at the $Li_{5.5}PS_{4.5}Cl_{1.5}$/LiTFSI-EMIMTFSI interface based upon FIB-SEM-EDX and time-resolved EIS, it is clear from XPS that there has been a chemical reaction between the two electrolytes to form a SLEI (Figure 3). Much like in the case of $Li_{5.5}PS_{4.5}Cl_{1.5}$/LiTFSI-DOL:DME, the S 2p region of the spectrum shows that sulfate (red) and sulfite (orange) species have been formed. However, in contrast, there is also evidence that P_2S_x (yellow) and Li_2S_x (brown) polysulfide species remain in the interphase layer, which is in keeping with the known insolubility of these species in ionic liquids. The high concentration of P_2S_x species within the interphase is confirmed in the P 2p region of the spectrum (yellow). The relative intensity and atomic percentage of chlorine-containing species observed is lower than in either the pristine sample or in the $Li_{5.5}PS_{4.5}Cl_{1.5}$/LiTFSI-DOL:DME sample. This is consistent that the work of Janek and co-workers, which suggests that the SLEIs can form layered structures with organic and salt decomposition products on the surface.[16] In this case, it is possible that $Li_{5.5}PS_{4.5}Cl_{1.5}$ and its decomposition products, such as LiCl, are buried beneath a layer which is composed primarily of organic decomposition products.

To test this hypothesis, HAXPES measurements were performed. In contrast to conventional XPS, the higher kinetic energy of photoelectrons enables depths of several tens of nanometres to be probed, enabling identification of chemical species buried within the SLEI. Chlorine is present exclusively in the $Li_{5.5}PS_{4.5}Cl_{1.5}$ solid electrolyte and its decomposition products; therefore, the Cl 1s signal serves as a probe for estimating the thickness of any overlying organic decomposition layer. To this end, the HAXPES survey spectra were analysed by examining the intensity of the Cl 1s core level peak relative to its inelastic background. A relatively intense inelastic background compared to the main Cl 1s peak indicates that the chlorine-containing species are located deeper beneath the surface. As shown in Figure 4a, the background-to-peak intensity ratio is significantly higher for $Li_{5.5}PS_{4.5}Cl_{1.5}$/LiTFSI-EMIMTFSI (orange) than for both the pristine sample (purple) and the $Li_{5.5}PS_{4.5}Cl_{1.5}$/LiTFSI-DOL:DME system (blue). Modelling of the background (see Experimental) yields an estimated chlorine-free overlayer thickness of ~21 nm for the former, which is substantially greater than that observed in the other samples (~3 nm). This suggests a layered structure to the SLEI, as shown in Figure 4b, with a thin overlayer of ionic liquid and salt decomposition products on the surface, and inorganic decomposition products buried more deeply.

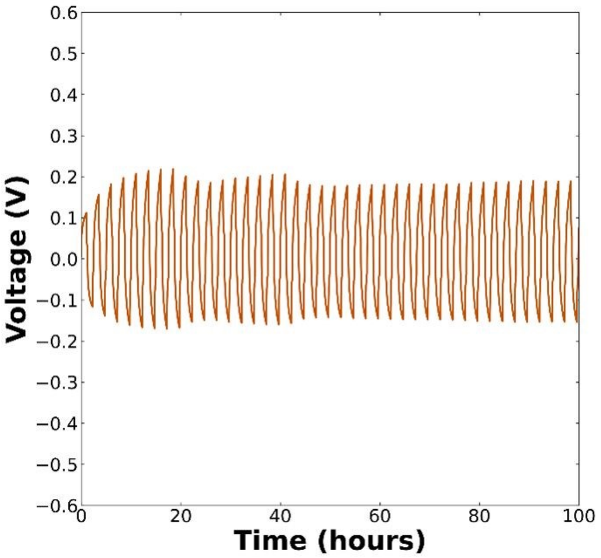

Figure 5: Galvanostatic cycling of a symmetric cell with the architecture: Li-In/LiTFSI-EMIMTFSI/$Li_{5.5}PS_{4.5}Cl_{1.5}$/LiTFSI-EMIMTFSI/Li-In at a current density of 0.1 $mA\cdot cm^{-2}$ for 100 hours.

Symmetric cell with $Li_{5.5}PS_{4.5}Cl_{1.5}$/LiTFSI-EMIMTFSI hybrid electrolyte

Given that the $Li_{5.5}PS_{4.5}Cl_{1.5}$/LiTFSI-EMIMTFSI interface shows relatively good stability when no current is being passed, we proceed to test the stability under dynamic cycling conditions. To achieve this, we cycle a symmetric cell with the architecture Li-In/LiTFSI-EMIMTFSI/$Li_{5.5}PS_{4.5}Cl_{1.5}$/LiTFSI-EMIMTFSI/Li-In. Li-In is chosen as the electrode material as it shows greater (electro)chemical stability and dendrite resistance than a Li metal anode, making this a good model system to study the evolution of the $Li_{5.5}PS_{4.5}Cl_{1.5}$/LiTFSI-EMIMTFSI SLEI while minimising secondary voltage effects of the Li-In/LiTFSI-EMIMTFSI interface.

Figure 5 shows cycling of the symmetric cell at a current density of 0.1 $mA\cdot cm^{-2}$ over 100 h. While the cell shows a small increase in voltage over the first 20 h of cycling, increasing to approximately 200 mV, the cell voltage then becomes stable. This observation suggests that the SLEI is similarly stable with dynamic cycling as when no current is passed, as the good stability with time is consistent with the time-resolved EIS (Figure 2b).

View Article Online
DOI: 10.1039/D5FD00058D

Conclusions

A stable interphase with a low area-specific resistance is of upmost importance when choosing a combination of a solid and liquid electrolytes for quasi-solid-state batteries. In this work, we characterise interphases between the sulfide-type solid electrolyte, $Li_{5.5}PS_{4.5}Cl_{1.5}$, and two different liquid electrolytes; LiTFSI-DOL:DME and LiTFSI-EMIMTFSI. Very different SLEIs are observed for these two systems. The $Li_{5.5}PS_{4.5}Cl_{1.5}$/LiTFSI-DOL:DME interphase is several microns thick, pitted, and composed of sulfates, sulfites and various organic decomposition produces. Expected polysulfide decomposition products were not observed, and we hypothesise that the dissolution of these species into the ether-based electrolyte is responsible for the thick and pitted SLEI morphology. The area-specific resistance of the interphase is observed to increase substantially over a 250 h period, reaching approximately 2,000 Ω·cm^2: substantially too high for practical quasi-solid-state batteries. The $Li_{5.5}PS_{4.5}Cl_{1.5}$/LiTFSI-EMIMTFSI interphase is very different in character. The interphase is considerably thinner and less resistive, reaching only 220 Ω·cm^2 before remaining stable over 250 h. XPS and HAXPES reveals that the SLEI has a layered structure, with a ~20 nm overlayer of ionic liquid and TFSI salt decomposition products covering a deeper layer of inorganic decomposition products. Symmetric cell cycling reveals that the SLEI remains relatively stable over electrochemical cycling, suggesting that this combination of electrolytes is appropriate for further study in quasi-solid-state Li-S batteries.

Experimental Section

$Li_{5.5}PS_{4.5}Cl_{1.5}$ solid electrolyte powder with a D50 of 2-3 µm was purchased from MSE Supplies and the phase was confirmed by powder X-ray diffraction (PXRD), Supplementary Figure 5. PXRD was performed using a Bruker D6 instrument with Co source, with a slit size of 0.5 mm. A step size of 0.0206° was used over a 2θ range of 10° to 90°, for a total collection time of 1 h. The expected phase, $Li_{5.5}PS_{4.5}Cl_{1.5}$, was confirmed by comparison against reference data, with a low concentration of impurities also observed.[38–41] The sample was prepared in an Ar glovebox and measurements were taken in a Bruker airtight holder.

Two liquid electrolytes are compared in this paper: 1 M LiTFSI in DOL-DME (1:1 v/v) (ELYTE), referred to as LiTFSI-DOL:DME; and 0.5 M LiTFSI in EMIMTFSI, referred to as LiTFSI-EMIMTFSI. The LiTFSI salt was purchased from TCI (>98.0 % purity) and the EMIMTFSI ionic liquid was from Proionic (electronic grade, ≥99.9 %w purity). Lithium-indium electrodes were prepared using lithium metal ribbon (Cambridge Energy Solutions) and indium foil (Thermo scientific, 99.99 % purity). The lithium and indium (thicknesses of 100 µm and 250 µm respectively) were folded and calendared to form a 100 µm Li-In alloy foil. All preparation was conducted in an Ar filled glovebox (H_2O, O_2 < 0.1 ppm).

Cross-sectional FIB-SEM was performed using a Thermo Fisher Scientific Helios G4 Plasma-FIB (focussed ion beam) instrument. Samples were transferred by airtight transfer holder to avoid exposure to air. The sectioning was performed at a voltage of 30 kV and a current of 15 nA. Scanning electron microscope (SEM) images were taken of the sectioned surfaces. Energy dispersive X-ray (EDX) was carried out using an X-max 150 silicon drift detector (Oxford Instruments) and analysed using the Aztec software package.

Potentiostatic electrochemical impedance spectroscopy (PEIS) was performed using a Biologic VMP3 potentiostat over a frequency range of 5 kHz to 50 Hz with a 10 mV voltage perturbation, collecting 10 points per decade. The 10 mm diameter $Li_{5.5}PS_{4.5}Cl_{1.5}$ solid electrolyte pellets were prepared by uniaxially pressing 205 mg of the powder at approximately 400 MPa. The cells were assembled in a custom Swagelock-type cell, using two stainless steel blocking electrodes. A controlled interfacial area was defined by PTFE O-rings with a 4 mm internal diameter. Measurements were taken at 25 °C over a 250 hour period. PEIS data were fitted using an equivalent circuit model on ZView software package.

Galvanostatic cycling was performed using a Biologic VMP3 potentiostat. Symmetric Li-In/LiTFSI-EMIMTFSI/$Li_{5.5}PS_{4.5}Cl_{1.5}$/LiTFSI-EMIMTFSI/Li-In cells were assembled in a 5 mm diameter PEEK cell within an Ar glovebox. The $Li_{5.5}PS_{4.5}Cl_{1.5}$ solid electrolyte was uniaxially cold pressed into the PEEK cell using 40 mg of powder at approximately 400 MPa. Glass microfibre disks (Whattman) were placed within the PEEK cell assembly, on either side of the $Li_{5.5}PS_{4.5}Cl_{1.5}$ solid electrolyte, and were soaked with 2 µL of liquid electrolyte. 5 mm diameter Li-In alloy electrode foils (100 µm thickness) and 5 mm diameter copper current collectors were then placed within the PEEK cell assembly before it was closed and placed under a pressure of approximately 10 MPa for cycling. Symmetric cell cycling was cycled at a current density of 0.1 mA·cm^{-2}, moving a capacity of 0.1 mA·h·cm^{-2} with each half cycle. Cycling was carried out at 25 °C for a 100 hour period.

Hard X-ray Photoelectron Spectroscopy (HAXPES) was performed using monochromated Ga Kα X-ray radiation (9252 eV, 3.57 mA emission at 250 W, micro-focussed to 50 µm, Excillum MetalJet) and an EW-4000 high voltage electron energy analyser (HAXPES-Lab, Scienta Omicron GmbH); the instrument has a base vacuum pressure of 5 x 10-10 mbar [1,2]. The entrance slit width used was 1.5 mm, and the pass energies used for survey and core level spectra were 500 and 100 eV respectively, with energy resolutions of 2.0 and 0.6 eV respectively.[42] The HAXPES instrument also has a monochromated Al Kα X-ray source (1486 eV, 20 mA emission at 300 W) for surface sensitive XPS at the same sample position, with a larger beam size of approx. 1 mm. Survey spectra and core levels were measured using 150 eV and 50 eV pass energy with energy resolutions of approx. 0.6 and 0.3 eV

View Article Online
DOI: 10.1039/D6FD00058D

respectively. XPS spectra binding energy scale calibration was performed using C 1s at 284.8 eV and HAXPES spectra binding energy scale calibration was performed using S 2p3/2 at 162.0 eV consistent with the XPS data. Analysis and curve fitting was performed using Voigt-approximation peaks using CasaXPS.[43] Core level relative sensitivity factors for HAXPES quantification were calculated according to[44,45]; for XPS quantification, Scofield factors were used. The background is modelled using the QUASES software package.[46] Inputs required in the QUASES-Analyze software include the inelastic mean free path which was calculated as approx. 13 nm for the Kinetic Energy of the Cl 1s core level (using the TPP2M formula[47] implemented in the QUASES package). Carbon was used as an approximate material for the overlayer given the complexity of the material system here; relative differences in an effective buried depth are valid but ultimate layer thicknesses are challenging to extract given the complex makeup of these surface overlayers.

Author contributions

J.J.M. contributed to all aspects of the research. S.K and B.S.F. carried out XPS and HAXPES experiments, analysed the data, and discussed the interpretation of the data. L.W. collected supplementary XPS data. L.Y. carried out cross-sectional FIB-SEM and EDX. M.P.S. contributed to interpretation of the EIS data. J.J.M. and D.S.J. wrote the draft with contributions from all authors. D.S.J. conceptualised and supervised the project.

Conflicts of interest

There are no conflicts to declare.

Data availability

All data are available for download from the University of Birmingham UBIRA eData repository.

Acknowledgements

The XPS and HAXPES work was supported by the EPSRC National Facility for XPS (“HarwellXPS”, EP/Y023587/1, EP/Y023609/1, EP/Y023536/1, EP/Y023552/1 and EP/Y023544/1) and the Henry Royce Institute for Advanced Materials, funded through EPSRC grants EP/R00661X/1, EP/S019367/1, EP/P025021/1 and EP/P025498/1. We acknowledge use of characterization facilities within the David Cockayne Centre for Electron Microscopy in the Department of Materials at the University of Oxford, and the Facility for Electron Microscopy in the School of Metallurgy and Materials at the University of Birmingham. We would also like to acknowledge the invaluable input provided by Energy Materials Group technician Ben Pye, who fabricated parts for the custom Swagelok-type cell.

References

1 P. G. Bruce, S. A. Freunberger, L. J. Hardwick and J.-M. Tarascon, *Nat. Mater.*, 2012, **11**, 19–29.
2 S. Gifford and J. Robinson, *Faraday Insights*, 2020, 1–5.
3 A. Jozwiuk, B. B. Berkes, T. Weiß, H. Sommer, J. Janek and T. Brezesinski, *Energy Environ. Sci.*, 2016, **9**, 2603–2608.
4 J. Janek and W. G. Zeier, *Nat. Energy*, 2016, **1**, 16141.
5 J. T. Kim, H. Su, Y. Zhong, C. Wang, H. Wu, D. Zhao, C. Wang, X. Sun and Y. Li, *Nature Chemical Engineering*, 2024, **1**, 400–410.
6 H. Huo and J. Janek, *Natl. Sci. Rev.*, 2023, **10**, nwad098.
7 Y. Shao, B. Pang, L. Bird, J. B. Robinson and P. R. Shearing, *John Wiley and Sons Inc*, 2026, preprint, DOI: 10.1002/aenm.202503239.
8 M. R. Busche, T. Drossel, T. Leichtweiss, D. A. Weber, M. Falk, M. Schneider, M. L. Reich, H. Sommer, P. Adelhelm and J. Janek, *Nat. Chem.*, 2016, **8**, 426–434.
9 A. Gupta, E. Kazyak, N. P. Dasgupta and J. Sakamoto, *J. Power Sources*, 2020, **474**, 228598.
10 T. Fuchs, B. Mogwitz, S.-K. Otto, S. Passerini, F. H. Richter and J. Janek, *Batter. Supercaps*, 2021, **4**, 1145–1155.
11 Z. Chen, G.-T. Kim, J.-K. Kim, M. Zarrabeitia, M. Kuenzel, H.-P. Liang, D. Geiger, U. Kaiser and S. Passerini, *Adv. Energy Mater.*, 2021, **11**, 2101339.
12 M. Weiss, B.-K. Seidlhofer, M. Geiß, C. Geis, M. R. Busche, M. Becker, N. M. Vargas-Barbosa, L. Silvi, W. G. Zeier, D. Schröder and J. Janek, *ACS Appl. Mater. Interfaces*, 2019, **11**, 9539–9547.
13 M. Schleutker, J. Bahner, C.-L. Tsai, D. Stolten and C. Korte, *Phys. Chem. Chem. Phys.*, 2017, **19**, 26596–26605.
14 J. Liu, X. Gao, G. O. Hartley, G. J. Rees, C. Gong, F. H. Richter, J. Janek, Y. Xia, A. W. Robertson, L. R. Johnson and P. G. Bruce, *Joule*, 2020, **4**, 101–108.

View Article Online
DOI: 10.1039/D6FD00058D

15 D. Spencer Jolly, D. L. R. Melvin, I. D. R. Stephens, R. H. Brugge, S. D. Pu, J. Bu, Z. Ning, G. O. Hartley, P. Adamson, P. S. Grant, A. Aguadero and P. G. Bruce, *Inorganics (Basel).*, 2022, **10**, 1–13.
16 M. R. Busche, M. Weiss, T. Leichtweiss, C. Fiedler, T. Drossel, M. Geiss, A. Kronenberger, D. A. Weber and J. Janek, *Adv. Mater. Interfaces*, 2020, **7**, 2000380.
17 B. Xu, H. Duan, H. Liu, C. Wang and S. Zhong, *ACS Appl. Mater. Interfaces*, 2017, **9**, 21077–21082.
18 L. Huang, H. Fu, J. Duan, T. Wang, X. Zheng, Y. Huang, T. Zhao, Q. Yu, J. Wen, Y. Chen, D. Sun, W. Luo and Y. Huang, *Chem*, 2022, **8**, 1928–1943.
19 F. Wei, S. Wu, J. Zhang, H. Fan, L. Wang, V. W. Lau, S. Hou, M. Zhang, J. Zhang, B. Liang and R. Zhao, *J. Mater. Chem. A*, 2021, **9**, 17039–17047.
20 B. Liu, Y. Gong, K. Fu, X. Han, Y. Yao, G. Pastel, C. Yang, H. Xie, E. D. Wachsman and L. Hu, *ACS Appl. Mater. Interfaces*, 2017, **9**, 18809–18815.
21 F. Langer, M. S. Palagonia, I. Bardenhagen, J. Glenneberg, F. La Mantia and R. Kun, *J. Electrochem. Soc.*, 2017, **164**, A2298–A2303.
22 Y.-N. Yang, F.-L. Jiang, Y.-Q. Li, Z.-X. Wang and T. Zhang, *Angew. Chem. Int. Ed.*, 2021, **60**, 24162–24170.
23 S. Yan, S. Abouali, C.-H. Yim, J. Zhou, J. Wang, E. A. Baranova, A. Weck, V. Thangadurai, A. Merati and Y. Abu-Lebdeh, *The Journal of Physical Chemistry C*, 2022, **126**, 14027–14035.
24 J. Leng, H. Wang, Y. Li, Z. Xiao, S. Wang, Z. Zhang and Z. Tang, *Appl. Surf. Sci.*, 2022, **575**, 151638.
25 S. Sarkar, B. Chen, C. Zhou, S. N. Shirazi, F. Langer, J. Schwenzel and V. Thangadurai, *Adv. Energy Mater.*, 2023, **13**, 2203897.
26 A. Shyamsunder, M. Palmer, I. R. Kochetkov, J. S. Sakamoto and L. F. Nazar, *ACS Appl. Mater. Interfaces*, 2023, **15**, 52571–52580.
27 W. Ma, Y. Guo, J. Sun, C. Zhang, Y. Zhu, H. Sun, L. Huang, Z. Hu, H. Wang, M. Zhu and G. Wang, *Angew. Chem. Int. Ed.*, 2025, **64**, e202418999.
28 K. “Kelvin” Fu, Y. Gong, S. Xu, Y. Zhu, Y. Li, J. Dai, C. Wang, B. Liu, G. Pastel, H. Xie, Y. Yao, Y. Mo, E. Wachsman and L. Hu, *Chemistry of Materials*, 2017, **29**, 8037–8041.
29 S. A. Pervez, G. Kim, B. P. Vinayan, M. A. Cambaz, M. Kuenzel, M. Hekmatfar, M. Fichtner and S. Passerini, *Small*, 2020, **16**, 2000279.
30 H. M. Woolley and N. M. Vargas-Barbosa, *Royal Society of Chemistry*, 2022, preprint, DOI: 10.1039/d2ta02179j.
31 H. M. Woolley, M. Lange, E. Nazmutdinova and N. M. Vargas-Barbosa, *ACS Energy Lett.*, 2024, **9**, 3547–3556.
32 D. L. R. Melvin, M. Siniscalchi, D. Spencer-Jolly, B. Hu, Z. Ning, S. Zhang, J. Bu, S. Marathe, A. Bonnin, J. Ihli, G. J. Rees, P. S. Grant, C. W. Monroe, T. J. Marrow, G. Li and P. G. Bruce, *Nat. Energy*, 2025, **10**, 1205–1214.
33 H. Lee, G. Kim, Y. Song, S. Cho and S. Park, *Adv. Funct. Mater.*, 2023, **33**, 2305373.
34 M. A. Philip, P. T. Sullivan, R. Zhang, G. A. Wooley, S. A. Kohn and A. A. Gewirth, *ACS Appl. Mater. Interfaces*, 2019, **11**, 2014–2021.
35 B. Fan, W. Li, Z. Luo, X. Zhang, H. Ma, P. Fan and B. Xue, *ACS Appl. Mater. Interfaces*, 2022, **14**, 933–942.
36 J. T. S. Irvine, D. C. Sinclair and A. R. West, *Advanced Materials*, 1990, **2**, 132–138.
37 J. Auvergniot, A. Cassel, D. Foix, V. Viallet, V. Seznec and R. Dedryvère, *Solid State Ion.*, 2017, **300**, 78–85.
38 W. Buehrer, F. Altorfer, J. Mesot, H. Bill, P. Carron and H. G. Smith, *Journal of Physics: Condensed Matter*, 1991, **3**, 1055.
39 S. Li, J. Lin, M. Schaller, S. Indris, X. Zhang, T. Brezesinski, C.-W. Nan, S. Wang and F. Strauss, *Angew. Chem. Int. Ed.*, 2023, **62**, e202314155.
40 C. J. Ridley, F. Orlandi, C. L. Bull, N. P. Funnell, J. K. Hinton, R. S. Perry, S. Hull and R. Wurr, *J. Mater. Chem. A Mater.*, 2025, **13**, 25335–25344.
41 G. I. Finch and S. Fordham, *Proceedings of the Physical Society*, 1936, **48**, 85.
42 A. Regoutz, M. Mascheck, T. Wiell, S. K. Eriksson, C. Liljenberg, K. Tetzner, B. A. D. Williamson, D. O. Scanlon and P. Palmgren, *Review of Scientific Instruments*, 2018, **89**, 073105.
43 N. Fairley, www.casaxps.com.
44 D. J. H. Cant, B. F. Spencer, W. R. Flavell and A. G. Shard, *Surface and Interface Analysis*, 2022, **54**, 442–454.
45 B. F. Spencer, S. Maniyarasu, B. P. Reed, D. J. H. Cant, R. Ahumada-Lazo, A. G. Thomas, C. A. Muryn, M. Maschek, S. K. Eriksson, T. Wiell, T.-L. Lee, S. Tougaard, A. G. Shard and W. R. Flavell, *Appl. Surf. Sci.*, 2021, **541**, 148635.
46 www.quases.com.
47 H. Shinotsuka, S. Tanuma, C. J. Powell and D. R. Penn, *Surface and Interface Analysis*, 2015, **47**, 871–888.
48 P. Naillou, A. Boulineau, E. De Vito, E. Lavanant and P. Azaïs, *Energy Storage Mater.*, 2025, **75**, 104050.
49 El Kazzi Mario, *EPJ Web Conf.*, 2022, **273**, 1001.
50 J. Li, Y. Li, T. Liu, S. Zhang, X. Li and L. Ci, *Adv. Funct. Mater.*, 2025, **n/a**, 2504546.
51 C. Fiedler, B. Luerssen, M. Rohnke, J. Sann and J. Janek, *J. Electrochem. Soc.*, 2017, **164**, A3742.

View Article Online
DOI: 10.1039/D6FD00058D

Data availability

All data are available for download from the University of Birmingham UBIRA eData repository.